



Cite this: DOI: 10.1039/d1cy00826a

Mechanistic understanding of methane-to-methanol conversion on graphene-stabilized single-atom iron centers†

Sungil Hong  and Giannis Mpourmpakis *

The functionalization of methane to value-added liquid chemicals remains as one of the “grand challenges” in chemistry. In this work, we provide insights into the direct methane-to-methanol conversion mechanisms with H_2O_2 as an oxidant on single Fe-atom centers stabilized on N-functionalized graphene, using first principles calculations. By investigating a series of different reaction paths on various active centers and calculating their turnover frequencies, we reveal that a H_2O_2 -mediated radical mechanism and a Fenton-type mechanism are energetically the most plausible pathways taking place on di- and mono-oxo centers, respectively. Due to the thermodynamic preference of the mono-oxo center formation over the di-oxo under reaction conditions, the Fenton-type mechanism appears to determine the overall catalytic activity. On the other hand, the hydroxy(oxo) center, which is thermodynamically the most favorable center, is found to be catalytically inactive. Hence, the high activity is attributed to a fine balance of keeping the active centers as oxo-species during the reaction. Moreover, we reveal that the presence of solvent (water) can accelerate or slow down different pathways with the overall turnover of the dominant Fenton-type reaction being decreased. Importantly, this work reveals the nature of active sites and a gamut of reaction mechanisms for the direct conversion of methane to methanol rationalizing experimental observations and aiding the search for room temperature catalysts for methane conversion to liquid products.

Received 10th May 2021,
Accepted 16th July 2021

DOI: 10.1039/d1cy00826a

rsc.li/catalysis

Introduction

Methane (CH_4), the simplest hydrocarbon, is one of the most important energy sources because of its vast reserves. Natural gas is one of the most widely used fuels having a generated energy of 3.8×10^{13} kWh in 2018 and is expected to reach 5.9×10^{13} kWh in 2050, accounting for 20% of primary energy consumption across the globe.¹ Taking into account the presence of other methane sources (e.g., crystalline hydrates,² shale gas,³ and biogas⁴), which have the potential to be fully utilized with advancements in technology and infrastructure, establishes methane as an undoubtedly vital feedstock in our future energy portfolio. Nevertheless, there are technical hurdles in transporting this gaseous C_1 feedstock from remote production locations to chemical plants for its utilization and chemical conversion. Thus, developing efficient methane conversion processes to transportable liquid products is a critical issue to reduce the cost of energy-intensive methane storage at low temperatures and high pressures.⁵ In particular, methanol (CH_3OH) is an ideal target

product, because it can be used as a diesel-blended fuel⁶ and in direct methanol fuel cells,⁷ as well as in commercial technology to produce C_{2+} hydrocarbons.^{8–10} The current industrial process to produce CH_3OH from CH_4 operates indirectly involving syngas production (a mixture of CO and H_2). Despite the high yields, syngas production suffers from high cost and low energy efficiency because of the high operating temperature (>850 °C) and large infrastructure, which limits the use of methanol in the fuel industry.^{11–14} Thus, many efforts have been made to discover industrially viable processes for the direct methane conversion to methanol over the past few decades. However, direct conversion is extremely challenging primarily due to the low intrinsic reactivity of CH_4 resulting from the strong C-H bonds and absence of a dipole moment, which necessitates harsh reaction conditions (e.g., high temperatures and reactive oxidative reagents).¹⁵ Unfortunately, the use of harsh conditions mostly leads to over-oxidation and/or very low selectivity to desired products, because of the higher reactivity of the latter than that of methane.^{14–16} Therefore, it is of high importance to discover catalytic systems that directly convert methane to methanol under mild conditions with low energy input and high selectivity.

From the pioneering studies by Staley,^{17,18} Freiser,^{19,20} Armentrout,^{21,22} Schwarz,^{23–25} and Yoshizawa^{26–28} in the

Department of Chemical Engineering, University of Pittsburgh, Pittsburgh, Pennsylvania 15261, USA. E-mail: gmpourmp@pitt.edu

† Electronic supplementary information (ESI) available. See DOI: 10.1039/d1cy00826a

1980s and 1990s, cationic transition metal oxides have been extensively investigated for C–H activation of unsaturated hydrocarbons in the gas phase, among which FeO^+ attracted particular interest. The biradical double bond of FeO^+ in the high spin ground state, which is produced from Fe^+ accepting an oxygen atom from N_2O , was revealed to be highly reactive for hydrogen abstraction from hydrocarbons.^{24,26} When methane is added as a reactant, the methyl group forms a Fe^+-C bond after C–H activation and then migrates to hydroxyl to produce methanol; this reaction is characterized by two important spin inversions from sextet to quartet and back to sextet.^{26–28} In turn, the discovery of biomimetic activity of iron complexes embedded in zeolites for hydrocarbon conversion by Panov *et al.*^{29,30} motivated extensive research on transition metals loaded on stable and porous supports. In particular, Fe-containing MFI, BEA, CHA, and AEI type zeolites have shown remarkable activity for selective partial oxidation of methane.^{31–38} Geometric constraints and confinement effects by zeolite microporous structures result in enhanced activity of the α -oxygen of the ferryl iron ($[\text{Fe}=\text{O}]^{2+}$) active center, showing a low C–H activation barrier for methane (≤ 0.3 eV).^{33–35,37} However, the strong hydrophilicity of zeolite frameworks leads to a strongly bound reaction product (methanol) inside the pores, limiting activity to a relatively high temperature regime (≥ 200 °C).^{32,37,38} This limitation might be overcome by using metal organic frameworks (MOFs), which are highly tunable microporous solid materials. However, currently Fe-loaded MOFs seem to be far from low-temperature applications: Fe(II) loaded on MOF-74 is unstable for a long time,^{39,40} Fe(II) on some MIL families requires overwhelmingly high oxidation energy,⁴¹ and Fe(III) on MIL-53 suffers from very low loading limitations.⁴²

Recently, a single Fe-atom catalyst stabilized by N atoms on graphene carbon nanosheets (FeN_4/GN) was reported to be active for selective CH_4 conversion to C_1 products with a very low CO_2 selectivity (6% for 10 h).⁴³ The authors showed that H_2O_2 oxidizes the Fe site to form active oxygenated sites that can convert CH_4 into CH_3OOH or CH_3OH , which can be further oxidized to HCOOH or HOCH_2OOH .⁴³ The energy barrier for the first C–H cleavage was so small that the reaction could proceed even at ambient temperature, avoiding over-oxidation.⁴³ This catalytic system is remarkably promising in that a non-precious metal (Fe) shows high activity and remains stable even longer than the other coordinatively-unsaturated metal systems because of the highly stable C–N bonds in N-doped graphene.⁴⁴ Furthermore, the graphene support is advantageous because not only it allows high dispersion of the stabilized FeN_4 centers, but also its carbon network enhances the catalytic activity of the active site.^{43,44}

Herein, driven by the aforementioned experimental discoveries we conduct a detailed computational study for methane activation and conversion on an FeN_4/GN catalyst. We specifically focus on obtaining a mechanistic

understanding of methane-to-methanol conversion in the presence of the oxidant, H_2O_2 , by investigating a series of possible reactions. We also consider solvent effects (water) to account for experimental conditions and report estimated turnover frequencies (TOFs) addressing the overall reactivity of the catalyst. Our results reveal the nature of the active center and provide an in-depth mechanistic understanding of methanol synthesis from methane. Overall, this work can further guide efforts on the discovery of energy efficient methods for methane conversion to liquids.

Computational details

Density functional theory (DFT) calculations were performed with the Gaussian 09 software package at the B3LYP/6-31G(d) level of theory.^{45–47} Benchmark calculations validate that the level of theory chosen can accurately capture the reported catalytic trends (see ESI†). All the geometries at local minima or saddle points were fully optimized and verified with the mode and number of imaginary vibrational frequencies (the transition state has one and the ground state does not have an imaginary frequency). Furthermore, intrinsic reaction coordinate (IRC) calculations⁴⁸ were carried out for the optimized transition states (TS) to confirm that they accurately connect the corresponding reactants and products. The catalyst system is composed of a central single Fe atom and 4 N atoms, surrounded by 26 C atoms with the graphene edges terminated by H atoms (Fig. S1†). In the lowest energy spin state (triplet) of the system, the C–C bond lengths vary between 1.37 and 1.43 Å, which is close to that of pure graphene (1.42 Å). The Fe–N bond length is 1.895 Å, which is consistent with previous reports.^{49,50} The Gibbs free energies of the elementary oxidation/hydroxylation reactions of the Fe site for the formation of active sites were calculated from eqn (1) and (2):

$$G_{\text{oxi}} = (G_{(\text{cat}-\text{O})} + G_{(\text{H}_2\text{O})}) - (G_{(\text{cat})} + G_{(\text{H}_2\text{O}_2)}) \quad (1)$$

$$G_{\text{hydroxy}} = G_{(\text{cat}-\text{OH})} - \left(G_{(\text{cat})} + \frac{1}{2} G_{(\text{H}_2\text{O}_2)} \right) \quad (2)$$

where $G_{(\text{cat})}$ stands for the Gibbs free energy of the catalyst before the reaction, and $G_{(\text{cat}-\text{O})}$ and $G_{(\text{cat}-\text{OH})}$ are those of the catalyst when the Fe site obtains one oxygen and hydroxyl, respectively. Also, $G_{(\text{H}_2\text{O})}$ and $G_{(\text{H}_2\text{O}_2)}$ represent the Gibbs free energies of H_2O and H_2O_2 molecules, respectively. The energy changes along the reaction pathways were described in terms of Gibbs free energy. Through all the Gibbs free energy calculations, enthalpy and entropy corrections were applied to the electronic energy assuming 1 atm and 298.15 K. Solvent effects were taken into consideration applying the conductor-like polarizable continuum model (CPCM)⁵¹ using water as the solvent, since the reaction experimentally takes place in the presence of water.⁴³ Turnover frequencies (TOFs) of different pathways were calculated based on the energetic span model of S. Kozuch and S. Shaik⁵² at room temperature.

Results and discussion

1. Active site formation

The FeN_4 center embedded on the graphene structure can be oxidized by the oxidant (H_2O_2), forming highly reactive oxygen sites,⁴³ as well as hydroxyl sites. To understand the active site nature, we calculated the oxidation and hydroxylation energies of the catalyst in the ground spin state as shown in Fig. 1. The detailed profiles of the active center formation in various spin states are presented in the ESI† (Fig. S2). Both the first oxidation and hydroxylation steps from the bare FeN_4/GN are exothermic, where the former is energetically more favorable. The second oxidation from the mono-oxo species is endothermic, while hydroxylation is slightly exothermic forming the hydroxy(oxo) center. The formation of the hydroxy(oxo) species is the most preferred among all considered (-1.77 eV), followed by the mono-oxo center (-1.71 eV). Two consecutive hydroxylation reactions result in the di-hydroxy center, which is also stable with a formation energy of -1.57 eV.

2. Methane-to-methanol conversion mechanisms

(1) **Di-oxo FeN_4/GN .** Even though our calculations demonstrate that the mono-oxo FeN_4/GN structure is more favorable than the di-oxo one, the latter is considered first as Deng *et al.*⁴⁴ suggested that the Fe site exists in a symmetrical $\text{O}=\text{Fe}=\text{O}$ structure. We investigated three different mechanisms of methane-to-methanol conversion on the triplet di-oxo structure as shown in Fig. 2 and S3. The di-oxo centers in triplet and quintet spin states are isoenergetic (Fig. S2†), but we confirmed that an intersystem crossing (ISC) will not alter the energetics in all pathways presented, since there were no transition states that were lower in energy in the high spin state (*i.e.* quintet). All mechanisms are radical-based as the first step is homolytic C–H bond cleavage through H abstraction by reactive O, resulting in the formation of a free methyl radical and a hydroxyl ligand (TS 1). The H abstraction has been regarded as a key step of methane activation by transition

metal oxide cations/complexes and enzymes. The energy required for the C–H cleavage step is 0.67 eV, which is comparable to relevant methane activation barriers that have been reported in literature (*i.e.*, homolytic C–H cleavage that involves free methyl radical formation): 0.76 eV on $\text{Fe}-\text{O}$ modified graphene,⁵³ 0.72 – 0.99 eV on $\text{Fe}-\text{ZSM-5}$,^{54,55} 0.72 eV on Fe -loaded MOF-74,³⁹ and 0.64 – 0.79 on Fe -loaded MIL families.^{41,42} The generated methyl radical, in turn, produces CH_3OH *via* reaction with hydroxyl (called “oxygen rebound process”), which was suggested to occur on heme iron containing enzymes (cytochrome P-450) and the non-heme iron center of soluble methane monooxygenase.^{25,56–58} This step has a very small reaction barrier (0.14 eV, TS 2). Thereafter, CH_3OH is desorbed to leave the Fe site exposed to H_2O_2 , which regenerates the oxo center (TS 3) and completes the catalytic cycle. Even though the cleavage of the strong C–H bond (which normally limits the methane activation) is facile (0.67 eV, TS 1), the whole cycle is limited by the energy-demanding O recovery step (1.24 eV, TS 3). In other words, the active site regeneration appears to govern the activity of the di-oxo FeN_4/GN catalyst for methane conversion through path 1a.

Mechanistically, there is no difference between path 1a and the pathway suggested to occur on the single non-heme Fe center stabilized on several MOF families.⁴¹ However, the di-oxo FeN_4/GN is more active than these MOFs since the latter require higher energy input to regenerate the active site from the N_2O oxidant (1.24 eV, TS 3. 1.45 eV), even though the C–H activation is energetically similar (0.67 eV, TS 1 *vs.* 0.62 eV).⁴¹ The di-iron complexes on $\text{Fe}-\text{ZSM-5}$ were also reported to homolytically dissociate the C–H bond of methane, but these intrinsically complicated systems involve multiple mechanisms to produce methanol.⁵⁵ On the other hand, the single Fe site in $\text{Fe}-\text{ZSM-5}$ catalyzes methane in a different pathway:³⁶ a hydroxymethyl ($\text{HO}-\text{Fe}-\text{CH}_3$) center is formed through a single C–H dissociation step, which in turn, produces methanol *via* recombination of methyl and hydroxyl. This mechanism is essentially similar to how metal oxide cations ($[\text{MO}]^+$) catalyze methane as suggested by Yoshizawa *et al.*^{26,27} The hydroxymethyl intermediate can also be generated on the iron-oxo centers of the FeN_4/GN catalysts. This non-radical type C–H dissociation, however, does not occur in the ground spin state (triplet). Furthermore, the activation energies of this C–H activation were found to be 2.89 and 2.35 eV on the mono-oxo and di-oxo centers, respectively (results not shown). Therefore, the pathways that involve the hydroxymethyl intermediate are ruled out in this study.

Since H_2O_2 is used as an oxidant, this energetically demanding active site recovery step (TS 3) can be bypassed. In an alternative pathway (path 1b, Fig. 2(b)), after the first C–H cleavage, the produced methyl radical can react with a H_2O_2 molecule (from the liquid phase) to produce CH_3OH and a hydroxyl radical with a small activation energy (0.60 eV, TS 4). The remaining hydroxyl radical attacks the H of the hydroxyl ligand on Fe, regenerating the active O site with a negligible reaction barrier (0.02 eV, TS 5). As a H_2O_2 molecule participates

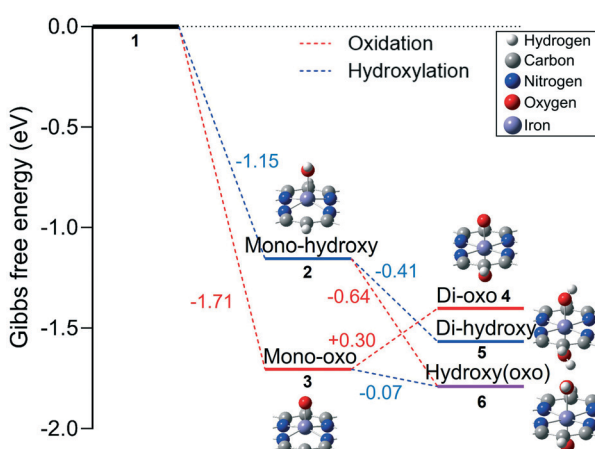


Fig. 1 Free energy profiles of formation of various active centers by oxidation/hydroxylation on the Fe center of the FeN_4/GN system.

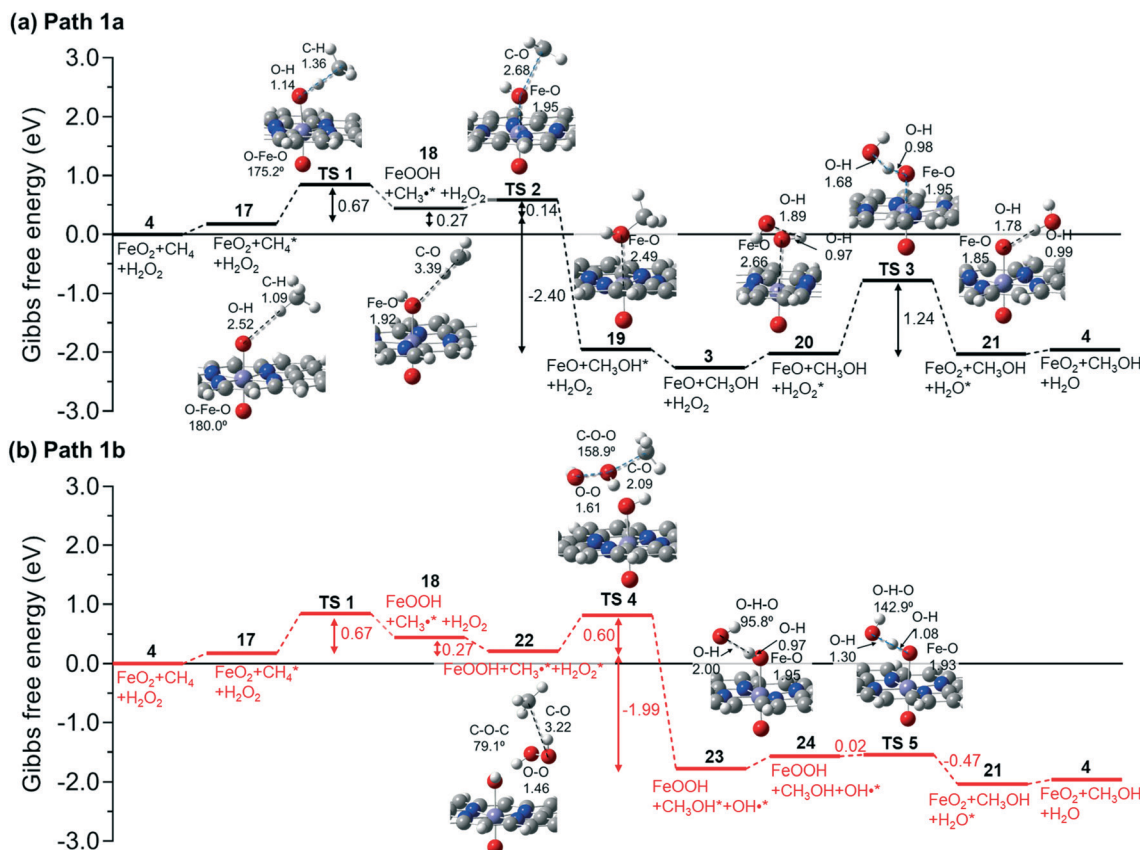


Fig. 2 Detailed free energy profiles of methane conversion to methanol by the di-oxo FeN_4/GN catalyst (triplet state) following (a) path 1a and (b) path 1b. “Fe” on the profiles stands for the FeN_4/GN catalyst structure, and “TS” represents the transition state. Asterisk (*) denotes the adsorbed species on the catalyst surface. The first four steps are identical in both pathways. Selected interatomic distances (in Å) are shown on the molecular structures.

in the middle of the pathway rather than simply recovering the active site as in path 1a, this pathway is characterized as H_2O_2 -mediated. Considering that the highest energy barrier in the whole cycle is only 0.67 eV for the C–H activation (TS 1), this pathway is energetically plausible, plus, there is an exothermic adsorption of H_2O_2 from the liquid phase (step 22) compared to path 1a. Nevertheless, the two identified transition states to produce methanol, *i.e.*, TS 2 in path 1a and TS 4 in path 1b, are competing as the reactants are essentially the same except for the additional H_2O_2 molecule in 22. Therefore, the ratio of intermediates (19 vs. 23) can be determined by the difference in the activation energies in accordance with the Curtin–Hammett principle.^{59,60} From the commonly shared intermediate (18), the energy barriers for TS 2 and TS 4 are 0.14 and 0.37 eV, respectively, which give the dominant population of intermediate 19 (6.74×10^3 times more than intermediate 23). In other words, most of the di-oxo centers will end up being in the mono-oxo form (3) as being trapped by the demanding active site recovery step (TS 3) instead of completing the cycle. This leads to the investigation of the mono-oxo center mechanisms, which will be presented in the following section.

Additionally, one more pathway on the di-oxo center is found as given in the ESI† (path 1c, Fig. S3), where the

produced methyl radical is stabilized by one of the N atoms surrounding the Fe center. Due to the larger reaction barriers (0.75 eV, TS 6 and 1.34 eV, TS 7), however, this pathway is less likely to occur than paths 1a and b. Also, a pathway with the singlet di-oxo FeN_4/GN catalyst (energetically unfavorable spin state) was investigated for comparison, which can be found in the ESI† (path 2, Fig. S4).

(2) Mono-oxo FeN_4/GN . As presented in Fig. 1 and S2,† our DFT calculations indicate the mono-oxo FeN_4/GN catalyst in the triplet spin state to be the second most stable form of the catalyst. This is in contrast to the computational results reported by Deng *et al.*,⁴⁴ where the di-oxo structure was energetically more stable than the mono-oxo. It should be noted that the thermodynamic preference of the mono-oxo over the di-oxo state, reported in Fig. S2,† can be further supported from an oxidation state perspective. The oxidation state of Fe at the FeN_4 center embedded in six-membered rings (or pyridinic FeN_4 site) is +2.^{49,50} This, in turn, increases to +4 and +6 forming mono-oxo ($\text{Fe}=\text{O}$) and di-oxo ($\text{O}=\text{Fe}=\text{O}$) centers, respectively. Despite the presence of $\text{Fe}(\text{vi})$ species in the highly oxidized form (*e.g.*, FeO_4^{2-}),⁶¹ this high oxidation state is relatively uncommon compared to the $\text{Fe}(\text{iv})$ -oxo complexes.⁶² This ferryl moiety ($\text{Fe}(\text{iv})=\text{O}$), in fact, has been identified as the active site of heme-containing

monooxygenases (cytochrome P-450)^{56,57} and Fe-ZSM-5 (ref. 34) for hydrocarbon activation. Finally, our mechanistic scenario in the previous subsection indicates that the di-oxo center will eventually be converted to the mono-oxo form, which is the thermodynamically most stable between the two forms. Under this consideration, we investigated the methane-to-methanol conversion mechanisms on the mono-oxo FeN_4/GN catalyst.

It becomes apparent that all reaction mechanisms considered in the di-oxo FeN_4/GN catalyst (Fig. 2 and S3†)

can take place on the mono-oxo as the single O-site exists in both cases. The equivalent pathways to paths 1a and b are presented as paths 3a and b in Fig. 3 (the counterpart of path 1c was not investigated due to the high TS energies involved). The activation energy for the first C–H cleavage from methane (1.58 eV, TS 10) is more than twice as high as that found on the di-oxo catalyst (0.67 eV, TS 1). The activation energy is lower than the value reported by T. Roongcharoen *et al.* (1.91 eV),⁶³ but both values are consistently high so that the O site on the mono-oxo catalyst is inactive at ambient

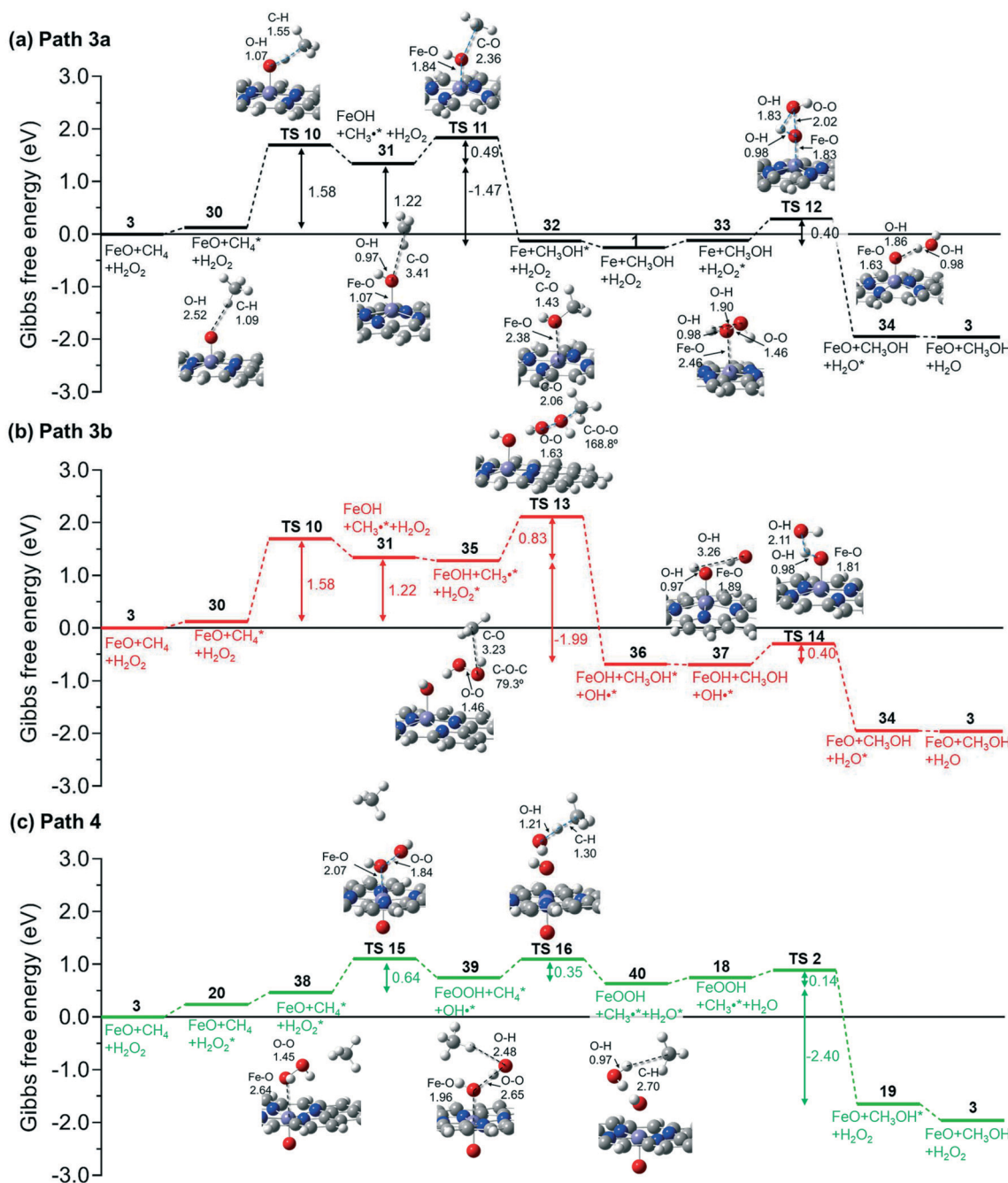


Fig. 3 Detailed free energy profiles of methane conversion to methanol by the mono-oxo FeN_4/GN catalyst (triplet state) following (a) paths 3a, (b) path 3b, and (c) path 4. Selected interatomic distances (in Å) are shown on the molecular structures.

temperature. This lower activity comes from the lower basicity of the active site, compared to that of the di-oxo center. The H affinity^{64,65} or H binding energy^{66–68} has been reported to be a descriptor for hydrocarbon activation *via* homolytic C–H bond cleavage. Here, we calculated the H atom binding energy (BE_H) from eqn (3) and related it to the activation energy for the homolytic C–H cleavage (ΔG_{C-H}) on all the active centers presented in Fig. 1. The BE_H and ΔG_{C-H} (Fig. 4) show a clear scaling relation, confirming the BE_H as a good descriptor for methane activation *via* homolytic C–H bond cleavage. This indicates that the O site on the mono-oxo catalyst has low activity because of its low basicity, while that of the di-oxo catalyst is a relatively strong base resulting in the facile C–H cleavage. Furthermore, we found a strong relationship between the oxidation state of the Fe centers and basicity of the active sites, in such a way that the basicity increases with the oxidation number of Fe from +3 (mono-hydroxy) to +6 (di-oxo). Notably, the mono-oxo and di-hydroxy centers form the same Fe(**iv**) oxidation state and have almost same BE_H of \sim 0.8 eV. The two different active sites of the hydroxy(oxo) center (Fe(**v**)) also show close basicity. These results reveal an interesting observation: the homolytic C–H dissociation of methane by the oxo or hydroxy active sites on the FeN₄/GN catalyst is modulated by the oxidation state of Fe, rather than a type of the active site.

$$BE_H = G_{(cat-H)} - G_{(cat)} - \frac{1}{2}G(H_2(g)) \quad (3)$$

Interestingly, the methane activation can potentially occur not only directly by O but also indirectly by Fe, which is exposed to the reactants at the non-oxidized side of the mono-oxo structure. Unlike paths 3a and b, this mechanism is initiated by H₂O₂ adsorption rather than C–H activation (path 4, Fig. 3(c)). A H₂O₂ molecule is adsorbed on the center

in such a way that one hydroxyl is closely bound to Fe while the other one is facing outwards. Overcoming a relatively small energy barrier (0.64 eV, TS 15), a hydroxyl radical is formed, simultaneously hydroxylating the Fe center. In turn, the produced hydroxyl radical abstracts H from CH₄ to generate water and a methyl radical (TS 16). Due to the highly active nature of the hydroxyl radical, the activation barrier for the homolytic C–H cleavage is only 0.35 eV. After water desorption, the methyl radical reacts with the remaining hydroxyl ligand to produce CH₃OH. The highest barrier corresponds to the O–O bond dissociation of H₂O₂ for OH radical generation at only 0.64 eV (TS 15). Indeed, it is known that CH₄ can be catalyzed into its oxygenates under mild conditions in the presence of H₂O₂ and O₂, where transition metals generate hydroxyl radicals from H₂O₂, and the radicals abstract H from CH₄ to produce methyl radicals;^{69–71} this is known as the Fenton-type reaction.⁷² This type of C–H activation has also been previously suggested to occur with a small barrier (0.77 eV) on an Fe–ZSM-5 catalyst.⁵⁵ Specifically, the authors reported that the dissociation of the O–O bond of H₂O₂ and methane activation *via* C–H cleavage took place in a single step.⁵⁵ Considering that methyl hydroperoxide (CH₃OOH), which is one of the major products from the Fenton-type methane oxidation,⁵⁵ was experimentally observed in large quantity,⁴³ the Fenton mechanisms seem plausible. However, Hammond *et al.*⁷³ reported that the mechanism of methane conversion to methanol with H₂O₂ by Cu-promoted Fe–ZSM-5 was different from the Fenton-type reaction. Further considering the complicated nature of Fenton chemistry,^{74,75} this highlights the challenge of elucidating radical chemistries.

It is worth noting that the structure obtained after water desorption in path 4 (18 in Fig. 3(c)) was already found in paths 1a–c (on the di-oxo catalyst). This shows that, instead of going through TS 2 as suggested in path 3, the produced methyl radical can react with H₂O₂ generating CH₃OH and OH radicals, steps which are found in path 1b (steps 22–TS 4–23). If this occurs, the mono-oxo center will be converted to the di-oxo configuration by being oxidized rather than acting as a catalyst, which indicates the possibility of the dynamic oxidation behavior of the Fe center. However, as also pointed out in the previous section, our statistical analysis based on the Boltzmann probability shows that this is not likely to occur. As shown in Fig. 1, the free energy of the mono-oxo is lower than that of the di-oxo by 0.30 eV, and this leads to the dominant population of the mono-oxo over di-oxo at 298.15 K. In an alternative pathway, the methyl radical can also be stabilized by N (as TS 6 in path 1c), but this pathway will be energetically demanding.

(3) **Hydroxy(oxo) FeN₄/GN.** Both the oxygen and hydroxyl active sites on the hydroxy(oxo) FeN₄/GN catalyst are shown to have a high activation energy for the initial C–H cleavage (around 1.2 eV) as presented in Fig. 4. Nonetheless, the bifunctional hydroxy(oxo) center may play an important role as one of the key species, because it is the most stable form of the catalyst (Fig. 1) and appears in the middle of

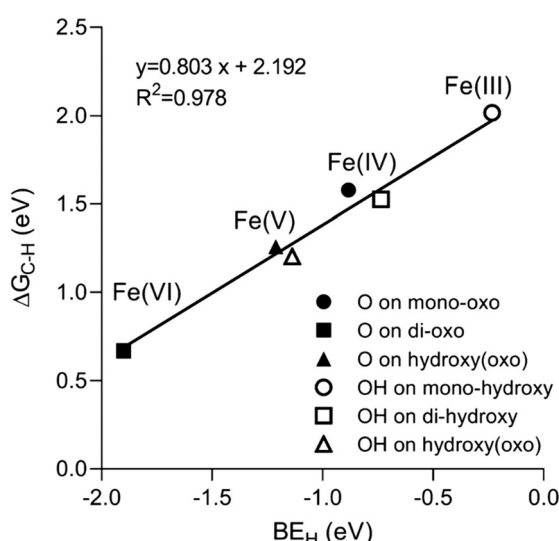


Fig. 4 Linear relationship between the H binding energy (BE_H) and the energy barrier for the homolytic C–H cleavage of methane (ΔG_{C-H}). The oxidation states of each Fe center are displayed along the data points.

reactions on oxo-catalysts along with adsorbed radical species (intermediate 18 in paths 1a and 4, and intermediate 23 in path 1b). Therefore, the mechanisms of methane-to-methanol conversion by the hydroxy(oxo) center are studied in detail. The catalysts in ground spin (doublet) and high spin (quartet) states are isoenergetic (Fig. S2†), and we found that ISC may occur in one pathway as discussed below.

All the pathways found on the di-oxo center can take place on the oxo site of the hydroxy(oxo) center: paths 5a and b in Fig. 5 correspond to paths 1a and b (Fig. 2), respectively (the counterpart of path 1c is not studied). Mechanistically, the only difference is that the hydroxyl radical produced by the reaction between the methyl radical and H_2O_2 in path 5b abstracts hydrogen from the hydroxylated center without any barrier (steps 47–45). Comparing the energetics, however, the hydroxy(oxo) center is distinctly different from the di-oxo center. Due to the low basicity of the active O site, the C–H activation is more demanding ($\Delta G_a = 1.27$ eV, TS 17), but the activation barrier for the regeneration of the active site from a H_2O_2 molecule is significantly decreased (1.24 eV, TS 3, path 1a \rightarrow 0.73 eV, TS 19, path 5a). Furthermore, as shown in Fig. S2,† the mono-hydroxy center (13) is more stable in the quartet spin state, which indicates that the system may

involve ISC between doublet and quartet spin states through TS 18, although the activation barrier of TS 18 is higher in quartet. In the high spin state, the active site recovery step is more facile (TS 19, $\Delta G_a = 0.43$ eV; note that this reported value can only be obtained with partial optimization relevant to the transition state). In turn, the facile active site recovery eliminates the advantage of the H_2O_2 -mediated mechanism (path 5b) over path 5a. The hydroxyl site of the hydroxy(oxo) center can also be an active site; another H_2O_2 -mediated mechanism is identified as shown in Fig. S5 in the ESI† (path 5c). However, except that the methanol production and active site recovery occur simultaneously (TS 22), path 5c is essentially the same as path 5b not only mechanistically but energetically, and thus the detailed description is omitted. Lastly, a concerted mechanism is found on the oxo site (path 5d, Fig. S5†), which corresponds to path 2 on the singlet di-oxo center. The high activation barrier (1.76 eV, TS 23) makes the pathway unlikely.

3. Solvent effects

In order to demonstrate how the water solvent affects the reaction mechanisms, the CPCM⁵¹ was applied on the

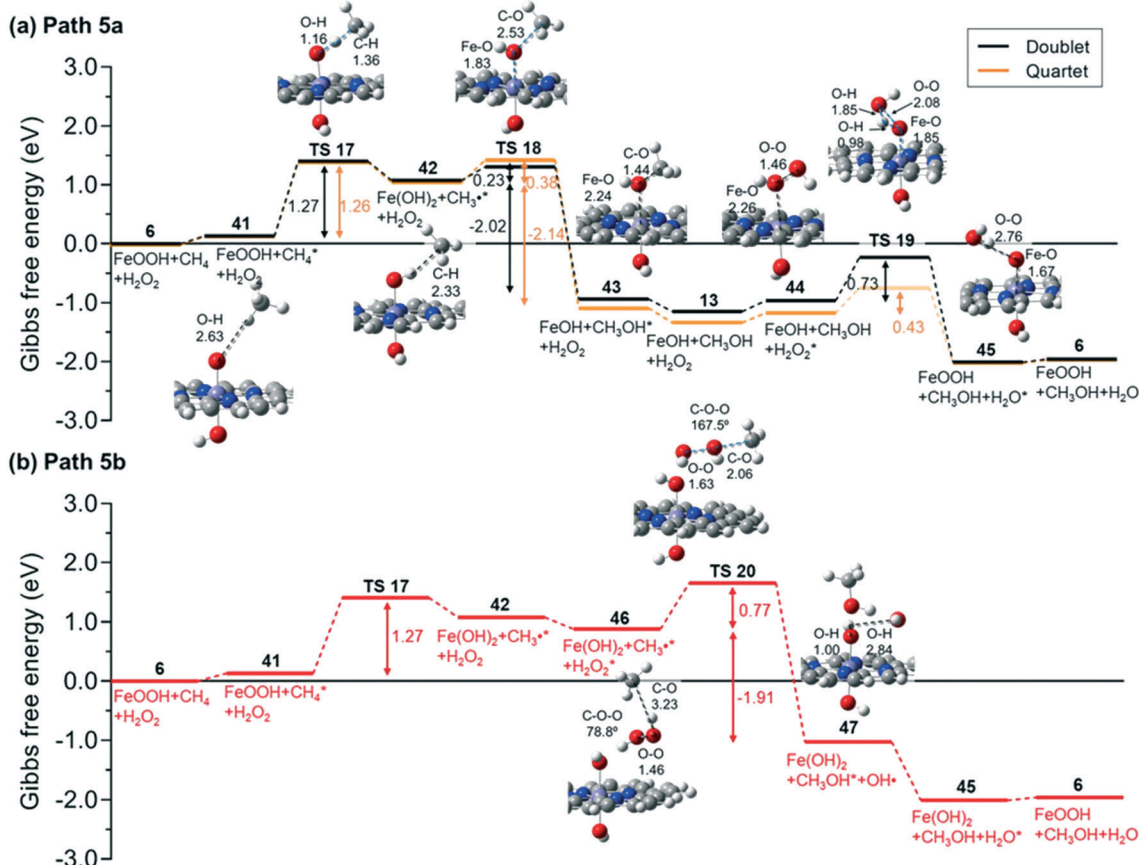


Fig. 5 Detailed free energy profiles of methane conversion to methanol by the hydroxy-oxo FeN_4/GN catalyst (doublet state) following (a) path 5a and (b) path 5b. The energy profile of path 5a in the high spin state (quartet) is also presented in panel (a) in orange. The TS 19 in quartet could not be located and the energy value was obtained with partial optimization. Selected interatomic distances (in Å) are shown on the molecular structures. In panel (a), only doublet structures are presented.

important pathways found on the di-oxo (paths 1a and b) and mono-oxo (path 4) FeN_4/GN catalysts, as shown in Fig. S6.[†] Solvent effects on the other pathways were not investigated because of their unfavorable energetics. Overall, the presence of the solvent does not modify the reaction mechanism, although the energetics of the elementary steps are affected. On the di-oxo center, the water desorption becomes exothermic (steps 21–4), because the polar water molecule is not favored to be adsorbed on the catalyst in the presence of the solvent. Likewise, desorption of produced CH_3OH on path 1b becomes more facile (steps 23–24). The remaining adsorption/desorption steps are practically unchanged. Importantly, all the reaction barriers in paths 1a and b decrease except for TS 2, which is still small although having doubled in the presence of water ($0.14 \text{ eV} \rightarrow 0.27 \text{ eV}$, TS 2). As a result, the methane-to-methanol conversion on the di-oxo center becomes more facile in the presence of water solvent. Nevertheless, the barrier for the O recovery is reduced slightly by 1.6% ($1.24 \text{ eV} \rightarrow 1.22 \text{ eV}$, TS 3) so that path 1a is still demanding in comparison to path 1b. It is worth noting that the change of the energetics alters the ratio of intermediates 19 *vs.* 23: from the shared state 18, the barrier for TS 2 is doubled while that for TS 4 is only slightly increased (by 0.07 eV) as solvent effects are considered. As a result, the population ratio of 19 to 23 is reduced by one order of magnitude (6.74×10^3 in the gas phase $\rightarrow 6.87 \times 10^2$ under water solvation), which means the contribution of path 1b to the overall activity increases, albeit it still remains small. In the case of path 4 on the mono-oxo center, the energy barrier for C–H cleavage by the OH radical is decreased in the presence of the solvent ($0.35 \text{ eV} \rightarrow 0.28 \text{ eV}$, TS 16). However, the rate-determining OH radical generation becomes less facile as the energy barrier increases ($0.64 \text{ eV} \rightarrow 0.76 \text{ eV}$, TS 15). Hence, the catalytic activity of the mono-oxo FeN_4/GN appears to decrease when considering solvent effects.

4. Energetic span model

Although the detailed reaction energy profiles presented so far provide quantitative information for each elementary step, they cannot rationalize the overall reaction pathway activity. The energetic span model provides accurate estimates of the TOF for a given catalytic cycle based on its detailed energetics.⁵² Thus, we calculated the TOFs of all the cycles investigated in this work as tabulated in Table 1. As expected, paths 1a and c show poor TOFs because of the large energy barriers involved. On the other hand, the TOF of path 1b is higher than those of paths 1a and c by more than 9 orders of magnitude in the gas phase, and increases by 80 times in the presence of solvent. This result clearly demonstrates that path 1b is the most efficient catalytic cycle on the di-oxo FeN_4/GN . Again, it must be noted that the results do not indicate that the di-oxo center is highly active, since path 1a is favored over 1b based on the Curtin–Hammett principle as discussed above. In the case of the mono-oxo center, the high

Table 1 Calculated turnover frequencies (TOFs) of the investigated pathways based on the energetic span model.⁵² The pathways investigated applying the CPCM solvation model⁵¹ are denoted as “sol”

Catalyst	Pathway	TOF (s^{-1})
Di-oxo	Path 1a	4.85×10^{-13}
	Path 1a-sol	7.19×10^{-13}
	Path 1b	1.49×10^{-3}
	Path 1b-sol	1.12×10^{-1}
	Path 1c	3.51×10^{-15}
Di-oxo (singlet)	Path 2	8.54×10^{-13}
Mono-oxo	Path 3a	9.65×10^{-19}
	Path 3b	2.19×10^{-23}
	Path 4	1.60×10^{-2}
	Path 4-sol	7.16×10^{-5}
	Path 5a	1.88×10^{-12}
Hydroxy(oxo)	Path 5b	1.23×10^{-16}
	Path 5c	1.50×10^{-19}
	Path 5d	1.13×10^{-20}

energy barrier for the homolytic C–H cleavage limits the TOFs of paths 3a and b at very low levels, but path 4 turns out to be very efficient, even more than path 1b. However, the calculated TOF of path 4 significantly decreases in the presence of water by more than 200 times, because of the increased barrier for the OH radical generation step (TS 15). The TOFs of the pathways on the singlet di-oxo and hydroxy(oxo) catalysts are extremely low as expected, so that they would not contribute to catalyzing the methanol synthesis reaction. As discussed, the path 5a on the hydroxy(oxo) center may involve ISC between low (doublet) and high (quartet) spin states. However, the probable ISC does not affect the TOF because the energy span of the pathway is essentially identical. Overall, in the gas-phase, the mono-oxo catalyst is the most active configuration as path 4 exhibits the largest TOF ($1.60 \times 10^{-2} \text{ s}^{-1}$), followed by the di-oxo center (path 1b, TOF: $1.49 \times 10^{-3} \text{ s}^{-1}$). On the other hand, in the presence of a solvated environment, the TOF of path 4 in the mono-oxo center decreases by more than 200 times (TOF: $7.16 \times 10^{-5} \text{ s}^{-1}$), while that of path 1b in the di-oxo center increases to be the most efficient pathway (TOF: $1.12 \times 10^{-1} \text{ s}^{-1}$). However, the population dominance of the mono-oxo center over the di-oxo is still valid in the presence of water based on the Boltzmann statistics, as the mono-oxo center is thermodynamically more favorable than the di-oxo. This suggests that the overall TOF is expected to be mostly contributed by the mono-oxo center. Combining these observations together, the solvated environment can unfavorably affect the overall catalytic efficiency. It is worth noting that the most active pathways among all (*i.e.*, paths 1b and 4) spend H_2O_2 as a reactant, rather than limiting its role for the active oxygen regeneration as reported in previous studies:^{43,44} H_2O_2 can directly react with a methyl radical to produce CH_3OH (path 1b – H_2O_2 -mediated mechanism), or be activated by the Fe center to form an OH radical, which can abstract H from CH_4 (path 4 – Fenton-type mechanism). This observation emphasizes the importance of the role of the oxidant in this specific reaction network.

Conclusions

In this work, we applied DFT calculations to investigate in detail the mechanisms of methane conversion to methanol using H_2O_2 on the single Fe-atom catalyst stabilized by N-functionalized graphene nanosheets (FeN_4/GN). Our results demonstrated that iron-oxo centers (mono-oxo and di-oxo) generated under reaction conditions can readily catalyze CH_4 even at ambient temperatures, whereas, the hydroxylated state of the catalyst is inert. By taking into consideration a number of different reaction pathways, catalyst configurations, and solvent effects, we revealed that reactive O-sites on the di-oxo catalyst are able to efficiently abstract H from CH_4 to generate a methyl radical (methane activation), which can further react with either the hydroxylated center or the oxidant H_2O_2 . As the reaction involves the energetically demanding O-site regeneration, however, the di-oxo catalyst is likely to be converted to the mono-oxo form. Compared to the di-oxo, the mono-oxo catalyst is thermodynamically more stable under reaction conditions, but the most active site appears to be the Fe center and not the oxygen site of the catalyst. The oxygen site is found to be inactive due to its low basicity, which stems from the oxidation state of the Fe center (+4). In contrast, the Fe center can catalyze methane to methanol through a Fenton-type mechanism by first dissociating the O–O bond of H_2O_2 to produce an OH radical, which in turn easily activates CH_4 and converts it to methanol. We revealed that the most feasible pathway on the mono-oxo catalysts consume the oxidant H_2O_2 as a reactant, not limiting its role to the active site regeneration as previously suggested. Solvent effects (presence of water) can either accelerate or slow down the methanol synthesis reaction depending on the mechanism and active center. However, considering the thermodynamic dominance of the mono-oxo centers and the mechanisms that take place on these centers, the presence of water solvent appears to reduce the overall catalytic activity. Taken together, our computational work sheds light into the methane-to-methanol conversion on the FeN_4/GN catalyst: there is a very complex interplay between thermodynamics of active site formation, solvent effects and competition of different reaction mechanisms. Our findings can potentially guide experimental efforts to discover efficient catalysts for converting methane to liquids under ambient conditions. In particular, our investigation regarding the solvation effects can be extended further to processes that involve a gas-phase oxidant instead of H_2O_2 , *e.g.*, N_2O ,⁴¹ O_3 ,⁷⁶ and O_2 ,⁵⁸ since such systems, depending on the operating conditions, can also be in a solvation environment of a polar liquid product (such as methanol). Future computational work in this area may include 1) the exploration of possible ligands that can block one face of the iron center in order to prevent the formation of the inactive hydroxyl site; 2) the introduction of explicit water molecules for more accurate investigation of water solvation effects; and 3) the use of microkinetic modeling for better understanding the complicated catalytic mechanisms.

Author contributions

G. M. conceived the project and S. H. performed all the calculations of this work. Both authors have contributed to the preparation of the manuscript.

Conflicts of interest

There are no conflicts to declare.

Acknowledgements

This work was supported by the National Science Foundation (NSF), under grant no. 1920623 and by the Central Research Development Funds (CRDF) of the University of Pittsburgh. The authors would like to acknowledge computational support from the Center for Research Computing at the University of Pittsburgh.

References

- International energy outlook 2019 with projections to 2050, <https://www.eia.gov/outlooks/ieo/pdf/ieo2019.pdf>, (accessed October 2020).
- S.-Y. Lee and G. D. Holder, *Fuel Process. Technol.*, 2001, **71**, 181–186.
- J. B. Curtis, *AAPG Bull.*, 2002, **86**, 1921–1938.
- K. C. Surendra, D. Takara, A. G. Hashimoto and S. K. Khanal, *Renewable Sustainable Energy Rev.*, 2014, **31**, 846–859.
- N. D. Parkyns, C. I. Warburton and J. D. Wilson, *Catal. Today*, 1993, **18**, 385–442.
- C. Sayin, *Fuel*, 2010, **89**, 3410–3415.
- S. Wasmus and A. Küver, *J. Electroanal. Chem.*, 1999, **461**, 14–31.
- M. Stöcker, *Microporous Mesoporous Mater.*, 1999, **29**, 3–48.
- U. Olsbye, S. Svelle, M. Bjørgen, P. Beato, T. V. W. Janssens, F. Joensen, S. Bordiga and K. P. Lillerud, *Angew. Chem., Int. Ed.*, 2012, **51**, 5810–5831.
- P. Tian, Y. Wei, M. Ye and Z. Liu, *ACS Catal.*, 2015, **5**, 1922–1938.
- A. P. York, T. Xiao and M. L. Green, *Top. Catal.*, 2003, **22**, 345–358.
- H. D. Gesser, N. R. Hunter and C. B. Prakash, *Chem. Rev.*, 1985, **85**, 235–244.
- J. R. Rostrup-Nielsen, J. Sehested and J. K. Nørskov, *Adv. Catal.*, 2002, **47**, 65–139.
- N. J. Gunsalus, A. Koppaka, S. H. Park, S. M. Bischof, B. G. Hashiguchi and R. A. Periana, *Chem. Rev.*, 2017, **117**, 8521–8573.
- R. Horn and R. Schlögl, *Catal. Lett.*, 2015, **145**, 23–39.
- R. H. Crabtree, *Chem. Rev.*, 1995, **95**, 987–1007.
- M. M. Kappes and R. H. Staley, *J. Am. Chem. Soc.*, 1981, **103**, 1286–1287.
- M. M. Kappes and R. H. Staley, *J. Phys. Chem.*, 1981, **85**, 942–944.
- B. S. Freiser, *Talanta*, 1985, **32**, 697–708.

20 T. C. Jackson, T. J. Carlin and B. S. Freiser, *J. Am. Chem. Soc.*, 1986, **108**, 1120–1126.

21 S. K. Loh, E. R. Fisher, L. Lian, R. H. Schulz and P. B. Armentrout, *J. Phys. Chem.*, 1989, **93**, 3159–3167.

22 D. E. Clemmer, Y.-M. Chen, F. A. Khan and P. B. Armentrout, *J. Phys. Chem.*, 1994, **98**, 6522–6529.

23 D. Schröder and H. Schwarz, *Angew. Chem., Int. Ed. Engl.*, 1990, **29**, 1433–1434.

24 A. Fiedler, D. Schroeder, S. Shaik and H. Schwarz, *J. Am. Chem. Soc.*, 1994, **116**, 10734–10741.

25 D. Schröder and H. Schwarz, *Angew. Chem., Int. Ed. Engl.*, 1995, **34**, 1973–1995.

26 K. Yoshizawa, Y. Shiota and T. Yamabe, *Chem. – Eur. J.*, 1997, **3**, 1160–1169.

27 K. Yoshizawa, Y. Shiota and T. Yamabe, *J. Am. Chem. Soc.*, 1998, **120**, 564–572.

28 K. Yoshizawa, Y. Shiota and T. Yamabe, *J. Chem. Phys.*, 1999, **111**, 538–545.

29 V. I. Sobolev, K. A. Dubkov, O. V. Panna and G. I. Panov, *Catal. Today*, 1995, **24**, 251–252.

30 G. I. Panov, V. I. Sobolev, K. A. Dubkov and A. S. Kharitonov, *Stud. Surf. Sci. Catal.*, 1996, **101**, 493–502.

31 A. Zecchina, M. Rivallan, G. Berlier, C. Lamberti and G. Ricciardi, *Phys. Chem. Chem. Phys.*, 2007, **9**, 3483–3499.

32 M. V. Parfenov, E. V. Starokon, L. V. Pirutko and G. I. Panov, *J. Catal.*, 2014, **318**, 14–21.

33 A. Rosa, G. Ricciardi and E. J. Baerends, *Inorg. Chem.*, 2010, **49**, 3866–3880.

34 B. E. Snyder, P. Vanelderen, M. L. Bols, S. D. Hallaert, L. H. Böttger, L. Ungur, K. Pierloot, R. A. Schoonheydt, B. F. Sels and E. I. Solomon, *Nature*, 2016, **536**, 317–321.

35 F. Goltl, C. Michel, P. C. Andrikopoulos, A. M. Love, J. Hafner, I. Hermans and P. Sautet, *ACS Catal.*, 2016, **6**, 8404–8409.

36 M. H. Mahyuddin, A. Staykov, Y. Shiota and K. Yoshizawa, *ACS Catal.*, 2016, **6**, 8321–8331.

37 M. H. Mahyuddin, Y. Shiota, A. Staykov and K. Yoshizawa, *Inorg. Chem.*, 2017, **56**, 10370–10380.

38 P. Sazama, J. Moravkova, S. Sklenak, A. Vondrova, E. Tabor, G. Sadovska and R. Pilar, *ACS Catal.*, 2020, **10**, 3984–4002.

39 P. Verma, K. D. Vogiatzis, N. Planas, J. Borycz, D. J. Xiao, J. R. Long, L. Gagliardi and D. G. Truhlar, *J. Am. Chem. Soc.*, 2015, **137**, 5770–5781.

40 D. J. Xiao, E. D. Bloch, J. A. Mason, W. L. Queen, M. R. Hudson, N. Planas, J. Borycz, A. L. Dzubak, P. Verma and K. Lee, *Nat. Chem.*, 2014, **6**, 590–595.

41 J. G. Vitillo, A. Bhan, C. J. Cramer, C. C. Lu and L. Gagliardi, *ACS Catal.*, 2019, **9**, 2870–2879.

42 D. Y. Osadchii, A. I. Olivos-Suarez, Á. Szécsényi, G. Li, M. A. Nasalevich, I. A. Dugulan, P. S. Crespo, E. J. Hensen, S. L. Veber and M. V. Fedin, *ACS Catal.*, 2018, **8**, 5542–5548.

43 X. Cui, H. Li, Y. Wang, Y. Hu, L. Hua, H. Li, X. Han, Q. Liu, F. Yang and L. He, *Chem.*, 2018, **4**, 1902–1910.

44 D. Deng, X. Chen, L. Yu, X. Wu, Q. Liu, Y. Liu, H. Yang, H. Tian, Y. Hu and P. Du, *Sci. Adv.*, 2015, **1**, e1500462.

45 M. J. Frisch, G. W. Trucks, H. B. Schlegel, G. E. Scuseria, M. A. Robb, J. R. Cheeseman, G. Scalmani, V. Barone, B. Mennucci, G. A. Petersson, H. Nakatsuji, M. Caricato, X. Li, H. P. Hratchian, A. F. Izmaylov, J. Bloino, G. Zheng, J. L. Sonnenberg, M. Hada, M. Ehara, K. Toyota, R. Fukuda, J. Hasegawa, M. Ishida, T. Nakajima, Y. Honda, O. Kitao, H. Nakai, T. Vreven, J. A. Montgomery, Jr., J. E. Peralta, F. Ogliaro, M. Bearpark, J. J. Heyd, E. Brothers, K. N. Kudin, V. N. Staroverov, T. Keith, R. Kobayashi, J. Normand, K. Ragavachari, A. Rendell, J. C. Burant, S. S. Iyengar, J. Tomasi, M. Cossi, N. Rega, J. M. Millam, M. Klene, J. E. Knox, J. B. Cross, V. Bakken, C. Adamo, J. Jaramillo, R. Gomperts, R. E. Stratmann, O. Yazyev, A. J. Austin, R. Cammi, C. Pomelli, J. W. Ochterski, R. L. Martin, K. Morokuma, V. G. Zakrzewski, G. A. Voth, P. Salvador, J. J. Dannenberg, S. Dapprich, A. D. Daniels, O. Farkas, J. B. Foresman, J. V. Ortiz, J. Cioslowski and D. J. Fox, *GAUSSIAN 09 (Revision D.01)*, Gaussian Inc., Wallingford, CT, 2013.

46 A. D. Becke, *J. Chem. Phys.*, 1992, **96**, 2155–2160.

47 C. Lee, W. Yang and R. G. Parr, *Phys. Rev. B: Condens. Matter Phys.*, 1988, **37**, 785–789.

48 C. Gonzalez and H. B. Schlegel, *J. Chem. Phys.*, 1989, **90**, 2154–2161.

49 J. Sun, Y. Fang and Z. Liu, *Phys. Chem. Chem. Phys.*, 2014, **16**, 13733–13740.

50 A. Titov, P. Zapol, P. Král, D.-J. Liu, H. Iddir, K. Baishya and L. A. Curtiss, *J. Phys. Chem. C*, 2009, **113**, 21629–21634.

51 V. Barone and M. Cossi, *J. Phys. Chem. A*, 1998, **102**, 1995–2001.

52 S. Kozuch and S. Shaik, *Acc. Chem. Res.*, 2011, **44**, 101–110.

53 S. Impeng, P. Khongpracha, C. Warakulwit, B. Jansang, J. Sirijaraensre, M. Ehara and J. Limtrakul, *RSC Adv.*, 2014, **4**, 12572–12578.

54 W. Liang, A. T. Bell, M. Head-Gordon and A. K. Chakraborty, *J. Phys. Chem. B*, 2004, **108**, 4362–4368.

55 Á. Szécsényi, G. Li, J. Gascon and E. A. Pidko, *ACS Catal.*, 2018, **8**, 7961–7972.

56 J. T. Groves, *J. Chem. Educ.*, 1985, **62**, 928–931.

57 V. W. Bowry and K. U. Ingold, *J. Am. Chem. Soc.*, 1991, **113**, 5699–5707.

58 P. C. Wilkins, H. Dalton, I. D. Podmore, N. Deighton and M. C. R. Symons, *Eur. J. Biochem.*, 1992, **210**, 67–72.

59 D. Y. Curtin, *Rec. Chem. Prog.*, 1954, **15**, 110–128.

60 J. I. Seeman, *Chem. Rev.*, 1983, **83**, 83–134.

61 H. Goff and R. K. Murmann, *J. Am. Chem. Soc.*, 1971, **93**, 6058–6065.

62 E. V. Rybak-Akimova, in *Physical Inorganic Chemistry Reactions, Processes and Applications*, ed. A. Bakac, Wiley, Hoboken, NJ, 2010, Mechanisms of oxygen binding and activation at transition metal centers, pp. 109–188.

63 T. Roongcharoen, S. Impeng, N. Kungwan and S. Namuangruk, *Appl. Surf. Sci.*, 2020, **527**, 146833.

64 A. A. Latimer, A. R. Kulkarni, H. Aljama, J. H. Montoya, J. S. Yoo, C. Tsai, F. Abild-Pedersen, F. Studt and J. K. Nørskov, *Nat. Mater.*, 2017, **16**, 225–229.

65 E. C. Tyo, C. Yin, M. Di Vece, Q. Qian, G. Kwon, S. Lee, B. Lee, J. E. DeBartolo, S. Seifert and R. E. Winans, *ACS Catal.*, 2012, **2**, 2409–2423.

66 H. Aljama, J. K. Nørskov and F. Abild-Pedersen, *J. Phys. Chem. C*, 2017, **121**, 16440–16446.

67 M. Dixit, P. Kostetskyy and G. Mpourmpakis, *ACS Catal.*, 2018, **8**, 11570–11578.

68 M. C. Cholewinski, M. Dixit and G. Mpourmpakis, *ACS Omega*, 2018, **3**, 18242–18250.

69 G. B. Shul'pin and G. V. Nizova, *React. Kinet. Catal. Lett.*, 1992, **48**, 333–338.

70 G. V. Nizova, G. Süss-Fink and G. B. Shul'pin, *Chem. Commun.*, 1997, 397–398.

71 G. Süss-Fink, G. V. Nizova, S. Stanislas and G. B. Shul'pin, *J. Mol. Catal. A: Chem.*, 1998, **130**, 163–170.

72 C. C. Winterbourn, *Toxicol. Lett.*, 1995, **82**, 969–974.

73 C. Hammond, M. M. Forde, M. H. Ab Rahim, A. Thetford, Q. He, R. L. Jenkins, N. Dimitratos, J. A. Lopez-Sanchez, N. F. Dummer and D. M. Murphy, *Am. Ethnol.*, 2012, **124**, 5219–5223.

74 B. Ensing, F. Buda and E. J. Baerends, *J. Phys. Chem. A*, 2003, **107**, 5722–5731.

75 A. S. Petit, R. C. R. Pennifold and J. N. Harvey, *Inorg. Chem.*, 2014, **53**, 6473–6481.

76 A. Božović, S. Feil, G. K. Koyanagi, A. A. Viggiano, X. Zhang, M. Schlangen, H. Schwarz and D. K. Bohme, *Chem. – Eur. J.*, 2010, **16**, 11605–11610.